








ZSCAN4⁺ mouse embryonic stem cells have an oxidative and flexible metabolic profile

Annaelena Troiano^{1,2,†}, Consiglia Pacelli^{3,†} , Vitalba Ruggieri⁴, Rosella Scrima³, Martina Addeo^{1,2}, Francesca Agriesti⁴, Valeria Lucci^{1,5}, Gina Cavaliere¹, Maria Pina Mollica¹, Marianna Caterino⁶, Margherita Ruoppolo⁶, Simona Paladino⁶ , Daniela Sarnataro⁶ , Feliciano Visconte⁷, Francesco Tucci³ , Piervito Lopriore³ , Viola Calabrò¹, Nazzareno Capitanio³, Claudia Piccoli^{3,*,‡}  & Geppino Falco^{1,2,5,‡,**} 

Abstract

Cultured mouse embryonic stem cells are a heterogeneous population with diverse differentiation potential. In particular, the subpopulation marked by *Zscan4* expression has high stem cell potency and shares with 2 cell stage preimplantation embryos both genetic and epigenetic mechanisms that orchestrate zygotic genome activation. Although embryonic *de novo* genome activation is known to rely on metabolites, a more extensive metabolic characterization is missing. Here we analyze the *Zscan4*⁺ mouse stem cell metabolic phenotype associated with pluripotency maintenance and cell reprogramming. We show that *Zscan4*⁺ cells have an oxidative and adaptable metabolism, which, on one hand, fuels a high bioenergetic demand and, on the other hand, provides intermediate metabolites for epigenetic reprogramming. Our findings enhance our understanding of the metastable *Zscan4*⁺ stem cell state with potential applications in regenerative medicine.

Keywords cell intermediate metastate; embryonic stem cells; heterogeneity; metabolism; pluripotency

Subject Categories Metabolism; Stem Cells & Regenerative Medicine

DOI 10.15252/embr.201948942 | Received 29 July 2019 | Revised 16 April 2020 | Accepted 22 April 2020 | Published online 18 May 2020

EMBO Reports (2020) 21: e48942

Introduction

Embryonic stem cells (ESCs) are pluripotent cell lines with the capacity of self-renewal and broad differentiation plasticity. They

are commonly derived from the inner cell mass of the mammalian blastocyst and are able to differentiate into all three germ layers and to infinitely self-replicate [1].

ESCs can be maintained *in vitro* as established cell lines. The establishment of an ESCs culture entails the liberation of pluripotent and self-renewing cells from the fated differentiation. However, in culture conditions, ESCs are not a homogeneous cellular population, but they are a mosaic of subpopulations in dynamic equilibrium expressing a distinct set of cell surface antigens and marker genes for pluripotency [2,3]. Interestingly, ESCs sporadically convert to the 2C-like cells that represent a small fraction of the cellular population with high pluripotency capabilities.

An interesting study has dissected the transition from ESCs to the 2 cell-like cells, identifying transitory intermediate subpopulations of cells expressing low, medium, and high levels of *Zscan4* transcription factor, respectively [4]. In the last years, relevant studies have elucidated the gene network underlying *Zscan4* metastate [5,6] and the complex epigenetic program related to its totipotent potential [4,7] confirming its significant implications for the early embryo development and cellular reprogramming field.

Development beyond the end of the 2-cell stage requires zygotic genome activation (ZGA) through *de novo* transcription regulation [8,9]. Such major reprogramming of the genome requires metabolites whose production is dependent on the mitochondrial enzymes driving the tricarboxylic acid (TCA) cycle and the utilization of pyruvate by pyruvate dehydrogenase [10]. Embryonic stem cells utilize elevated aerobic glycolysis for energy generation [11]; however, as pluripotent cells commit to one of the three embryonic germ layers, glycolytic flux decreases and OXPHOS becomes important for energy generation [12].

1 Department of Biology, University of Naples Federico II, Naples, Italy

2 Istituto di Ricerche Genetiche Gaetano Salvatore Biogem Scarl, Ariano Irpino, Italy

3 Department of Clinical and Experimental Medicine, University of Foggia, Foggia, Italy

4 Laboratory of Pre-Clinical and Translational Research, IRCCS-CROB, Referral Cancer Center of Basilicata, Rionero in Vulture, Italy

5 IEOS-CNR, Institute of Experimental Endocrinology and Oncology "G. Salvatore" - National Research Council, Naples, Italy

6 Department of Molecular Medicine and Medical Biotechnology, University of Naples Federico II, Naples, Italy

7 CEINGE Biotecnologie Avanzate s.c.a.r.l., Napoli, Italy

*Corresponding author. Tel: +39 0881 588060; E-mail: claudia.piccoli@unifg.it

**Corresponding author. Tel: +39 081 679092; E-mail: geppino.falco@unina.it

†These authors contributed equally to this work as first authors

‡These authors contributed equally to this work as senior authors

Recently, we showed that retinoic acid (RA) enhances the exit of ESCs toward 2 cell-like cells and sustains pluripotency by enhancing *Zscan4* high intermediate subpopulation [13].

Since little is known about metabolic switching during the transition between ESC toward 2 cell-like cells, here we aimed to define the metabolism of RA-derived *Zscan4* ESCs subpopulation, known driver of cell fate and able to affect pluripotency maintenance and cell reprogramming.

In this paper, we report data linking *Zscan4* metastate to oxidative metabolism driven from substrates alternative to glucose, glutamine, and fatty acids.

Results and Discussion

Arg2 expression in *Zscan4* ESCs metastate

Arg2 is a mitochondrial protein that catalyzes the hydrolysis of arginine to ornithine and urea, completing the last step of the urea cycle [14]. Differential gene expression analyses, by microarrays, showed an impressive increase of *arg2* expression (about 34 folds) in *Zscan4*⁺ ESCs compared to *Zscan4*⁻ ESCs [15]. We validated this data by measuring *arg2* expression in *Zscan4*⁺ and *Zscan4*⁻ ESCs by qPCR. Transgenic ES^{*Zscan4*_Emerald} cells were cultured in RA for 3 days and sorted based on the green fluorescence of the Emerald reporter [16]. According to microarrays data, in *Zscan4*⁺ cells *arg2* mRNA transcript level was 40-fold higher (Fig 1A) and *arg2* protein was exclusively detected in *Zscan4*⁺ subpopulation by immunoblot analysis (Fig 1B). In order to investigate the role of *arg2* enzyme in *Zscan4*⁺ subpopulation properties, we performed RNA interference experiments to downregulate *Arg2* transcripts expression in ESCs (Fig 1C). Downregulation efficiency in sorted *Zscan4*⁺ cells respect to *Zscan4*⁺ siCtrl was measured both at mRNA and protein level and reported in Fig 1D. Since histonic protein H3 is a key feature of *Zscan4*⁺ metastate [17,18], we evaluated the chromatin condensation state by staining the cells with an anti-H3 antibody (revealed by a secondary FITC-conjugated antibody) followed by imaging flow cytometer analyses (see Materials and Methods). Remarkably, *Zscan4*⁺siArg2 displayed higher fluorescence signal compared with *Zscan4*⁺siCtrl in nuclear region defined by DAPI labeling (about 316,000 versus 249,000, $n > 1,400$ cells), suggesting a higher condensation state upon *Arg2* knockdown. Moreover, to better analyze the distribution of fluorescence signal, we applied the modulation feature method, which measures the fluorescence intensity range of an image (see Materials and Methods). Interestingly, we observed that H3 fluorescent signal displays both homogenous and clustered pattern. On this basis, we have distinguished two cell subpopulations: the population R1, where H3 signal is more homogeneously distributed, and the population R2, where it is more clustered and, therefore, corresponding to higher DNA condensation. As shown in Fig 1E, the percentage of cells exhibiting clustered pattern is significantly higher upon *Arg2* knockdown (22% versus 15%, $n > 1,400$ cells), further supporting a larger chromatin condensation state in *Zscan4*⁺siArg2 cells respect to the control. This observation suggests a role of *Arg2* in maintaining the undifferentiated state.

Measurement of metabolic fluxes and mitochondrial respiration-linked parameters in *Zscan4*⁻ and *Zscan4*⁺ cells

To better characterize the metabolic state of *Zscan4*⁺ ESCs, cultured in RA for 3 days, we measured the main metabolic fluxes running in *Zscan4*⁻ and *Zscan4*⁺ cells, using the Seahorse technology. The mitochondrial oxygen consumption rate (OCR), a reliable readout of mitochondrial activity, was significantly higher in *Zscan4*⁺ cells as compared with *Zscan4*⁻ control cells (Fig 2A). Conversely, the extracellular acidification rate (ECAR), which is a measure of the glycolytic activity, was only marginally changed (Fig 2B). Moreover, *Zscan4*⁺ cells had a higher OCR/ECAR ratio both under basal and maximally stimulated conditions (Fig 2C) and a larger NAD⁺/NADH ratio (Fig 2D).

Confocal microscopy imaging of cells loaded with the mitochondrial potential ($\Delta\Psi_m$)-sensitive probe TMRE confirmed, on an average basis, a significantly larger $\Delta\Psi_m$ -related fluorescence signal in *Zscan4*⁺ cells, despite the cellular heterogeneity (Fig 2E). These results indicate that *Zscan4*⁺ cells had shifted toward a more oxidative phenotype.

Moreover, we carried out a systematic analysis to investigate the possible differential expression of genes involved in the mitochondrial oxidative phosphorylation system in *Zscan4*⁺ and *Zscan4*⁻ cells. By using selective antibodies cocktail, we assessed by Western blotting the protein level of subunits of the respiratory chain complexes and ATP synthase. The results obtained did not show significant changes in the protein content of any of the OXPHOS complexes. However, a modest increase in the expression of representative mitochondrial genes in *Zscan4*⁺ cells detected by RT-PCR was observed (Fig EV1A). Moreover, we did not observe significant changes in the mitochondrial membrane integrity as evaluated by WB of specific markers (i.e. porin for outer membrane, cyclophilin D for matrix, cytochrome c for intermembrane space, complexes V and III subunits for inner membrane) (Fig EV1B and C). Finally, we analyzed the expression of factors involved in the mitochondrial dynamics (i.e. MFN1/2 and OPA1 for fusion, DRP-1 for fission). Again, no significant differences were observed in *Zscan4*⁺ cells compared to *Zscan4*⁻ cells. Similar results were observed for TOMM20 and TOMM40 routinely used to evaluate the mitochondrial mass (Fig EV1D and E). Altogether, these pieces of evidence would suggest that the metabolic shift versus a more oxidative phenotype observed in *Zscan4*⁺ cells is likely linked to a post-translational control of the OXPHOS machinery and/or to changes in the catabolic pathways upstream of it. This is consistent with the short frame time adaptation to the transient ZSCAN4 gene expression. Further investigations are needed to disentangle the mechanistic aspect of this issue.

Concerning the morphology of the mitochondrial compartment, we did not detect any particular difference between the two mES cell phenotypes neither using the MitoTracker Green probe (Fig 3A) nor by transmission electron microscopy analysis (Figs 3B and EV2). Notably, when the intracellular redox tone was investigated by the reactive oxidant species (ROS)-sensitive probe DCF, a significantly higher fluorescence signal was observed in *Zscan4*⁺ cells with the brighter intensity localized in an intracellular pattern resembling the mitochondrial network (Fig 3C).

Next, we sought to evaluate the relative contribution of different catabolites fueling the mitochondrial respiration chain. In cultured

cells, the major respiratory substrates are glutamine (Gln), fatty acids (FA), and glucose (Glc). Figure 4A unveils that treatment of the two stem cells phenotypes with a cocktail of inhibitors resulted in similar reliance of the basal OCR on the three aerobic substrates irrespective of whether respiration was sustained by endogenous or exogenously supplemented substrates. However, other unidentified

metabolites, likely constituted by short-/middle-chain FA and/or amino acids other than Gln, contributed to the overall respiratory activity both in *Zscan4*⁻ and *Zscan4*⁺ cells with the latter exhibiting a significantly larger Gln/FA/Glc-independent respiratory activity.

To further characterize the specific contribution of either of Gln, FA, Glc to mitochondrial respiration, we determined the OCR with

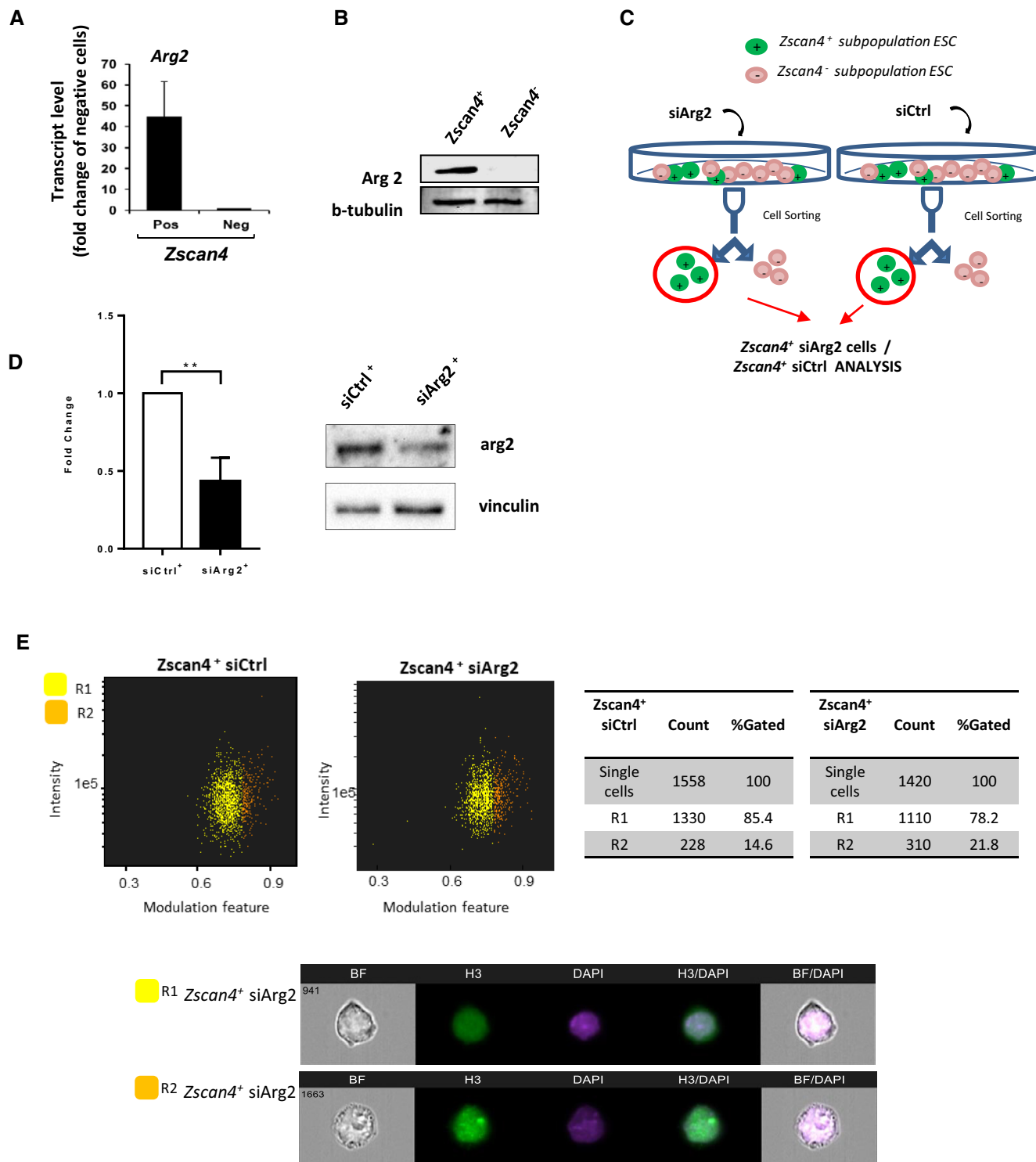


Figure 1.

Figure 1. *arg2* expression in *Zscan4* ESCs metastate.

- A Transgenic ES^{Zscan4⁺Emerald} cells were sorted, and total RNAs were extracted and subjected to RT-qPCR. The graph shows the mRNA expression level of *Arg2* in ES subpopulations.
- B Transgenic ES^{Zscan4⁺Emerald} cells were sorted, and total proteins were extracted and subjected to immunoblotting. The image is a representative of three independent biological Western blotting analysis on *arg2* expression in sorted ES^{Zscan4⁺Emerald} and control cells.
- C Schematic illustration of *Arg2* silencing and magnetic separation of the *Zscan4*⁺ cells. The modified ES^{Zscan4⁺LNGFR} cells were transfected with a siRNA that specifically target mouse *Arg2*. 96 h after siRNA transfection, cells were harvested and incubated with a LNGFR magnetically labeled antibody. Positive fractions were collected through autoMacs Separator. All the analyses were performed on *Zscan4*⁺ siArg2 and *Zscan4*⁺ siCtrl cells.
- D Transcript (left panel) and protein expression (right panel) levels of *Arg2* in ES^{Zscan4⁺LNGFR} cells after transfection with a non-silencing siRNA (siCtrl) or siRNA against *Arg2* (siArg2).
- E Imaging flow cytometry analysis on *Zscan4*⁺ siArg2 and *Zscan4*⁺ siCtrl cells. Samples were stained by labeling histone H3 protein. The intensity of H3 fluorescent signal was measured in the nuclear region by creating a mask defined by DAPI staining. The texture feature of fluorescent signal was analyzed by using the modulation method (for details see Materials and Methods). Two cell populations (R1 and R2) correspond to two different patterns of fluorescent signal: homogenous and clustered distribution, respectively.

Data information: Student's *t*-test was used for the statistical analysis in panels (A, B, D, and E). Bar values are means \pm SD of $n = 3$ independent biological replicates; * $P < 0.05$; ** $P < 0.01$ based on NEJM decimal format.

endogenous respiratory substrates by interchanging the addition of an inhibitor of a target pathway with that combining inhibitors of the other two alternative pathways. The inhibitors used were as follows: BPTES, an inhibitor of glutaminase; etomoxir, an inhibitor of long-chain fatty acid β -oxidation (FAO); UK5099, an inhibitor of the mitochondrial pyruvate carrier.

By performing such analysis, it was possible to estimate whether the cell strictly relies on a metabolic pathway (*dependency*) as well as its capacity to shift on a different metabolic pathway (*flexibility*). In particular, dependency indicates the relative amount of basal mitochondrial oxidation from a single fuel that cannot be compensated through oxidation of the other two fuels while capacity is the relative ability of a cell to oxidize a specific fuel in the basal state when oxidation of the other two fuels are blocked. Flexibility is the difference between capacity and dependency and indicates the relative ability of a cell in the basal state to switch or compensate mitochondrial oxidation from one fuel to another. As shown in Fig 4B, the basal OCR dependency of *Zscan4*⁺ to either of Gln, FA, and Glc was lower than that in *Zscan4*⁻, while the flexibility toward their utilization was larger; this was statistically significant for long-chain FA and pyruvate (Glc).

Moreover, we focused our studies on *Zscan4*⁺ cells cultured in RA conditions performing a quantitative analysis of different intracellular metabolites by LC-MSMS. Evaluation of free amino acid content in *Zscan4*⁺ and *Zscan4*⁻ ESC revealed a significant reduction of arginine level in *Zscan4*⁺ cells (7.9 ± 0.4 versus 4.3 ± 1.1 μ M; $P < 0.01$, $n = 6$ for each experimental group; final concentrations were calculated based on 0,1 mg protein from the cellular extract) with a concomitant slight increase of ornithine (Fig 4C). Furthermore, methionine and aspartic acids were also significantly enhanced in *Zscan4*⁺ cell subpopulation (8.5 ± 0.01 versus 34.8 ± 5.5 , $P < 0.01$, $n = 6$ for each experimental group for methionine and 63.1 ± 0.03 versus 83.4 ± 9.8 , $P < 0.05$, $n = 6$ for each experimental group for aspartate) (Fig 4C). Moreover, we profiled the acylcarnitine (AC) content in both the mESCs phenotypes by LC-MSMS (Table 1). The result reported in Fig 4D shows statistically significant higher levels of C14 (tetradecanoylcarnitine), C16 (hexadecanoylcarnitine), C18 (octadecanoylcarnitine) while C4 (butyrylcarnitine), C5 (isovalerylcarnitine), C6 (hexanoylcarnitine), and C8 (octanoylcarnitine) were lower. A higher content of C3 (propionylcarnitine) was observed in *Zscan4*⁺ cells and no differences in

C0 (free carnitine) and C2 (acetylcarnitine). Considering that the measured content of the ACs reflects their steady-state level, resulting from the balance between mitochondrial production/uptake and utilization, these data indicate that *Zscan4*⁺ cells are characterized by a selective reduction in the oxidation of long-chain FA in favor of that of short-/middle-chain FA.

Overall, the above-reported results indicate that in RA culture conditions *Zscan4*⁺ cells compared with *Zscan4*⁻ cells are hallmarked by a more oxidative and more adaptable/flexible metabolism.

Finally, to verify whether RA treatment per se has an effect on the metabolic asset observed in *Zscan4*-positive cells, we performed the featuring of the metabolic profile and mass spectrometry analysis of metabolites in *Zscan4*⁺ cells cultured in regular medium RM. In absence of retinoic acid, there are no significant changes in mitochondrial respiration and glycolysis (Fig EV3A) and in methionine or acylcarnitine levels (Fig EV3B and C). To better highlight the differences between RA and RM conditions, we compared the analysis of metabolites performed by mass spectrometry in *Zscan4*⁺ cells sorted in RM with *Zscan4*⁺ cells sorted in RA conditions. As expected, Fig EV4 shows a highly significant increase of specific amino acids detected in *Zscan4*⁺ cells sorted in RA compared to *Zscan4*⁺ cells sorted in RM conditions, thus suggesting a role of some amino acids in *Zscan4*⁺-RA cells characterized by high reprogramming capacity. It should be emphasized that when we compare *Zscan4*-positive versus negative cells in RA conditions, some differences are blurred likely because RA affects also *Zscan4* negative cells making some of them “younger” and closer to the positive ones. RA has been shown to push cells into the pluripotency state; in other words, the negative cells population remain heterogeneous but most of them, following RA treatment, are primed to *Zscan4*^{+low} cell intermediate.

Importantly, the pathway (metabolites) enriched in *Zscan4*⁺ cultured in RA, but not enriched in *Zscan4*⁺ sorted in conventional cell medium validated and consolidated our baseline approach reliability.

Featuring the metabolic profile of *Zscan4*⁺ mESC

Collectively, our data, schematically represented in Fig 5, show that different subsets of *ZSCAN4*-positive cells are characterized

by specific metabolic features. Stem cells need to continuously adapt to environmental changes to preserve their differentiation potential over time. Beyond energy production, it is well known

that mitochondrial homeostasis plays an important role in stem cell biology at the interface between environmental cues and the control of epigenetic identity [19,20]. Metabolic variations are not

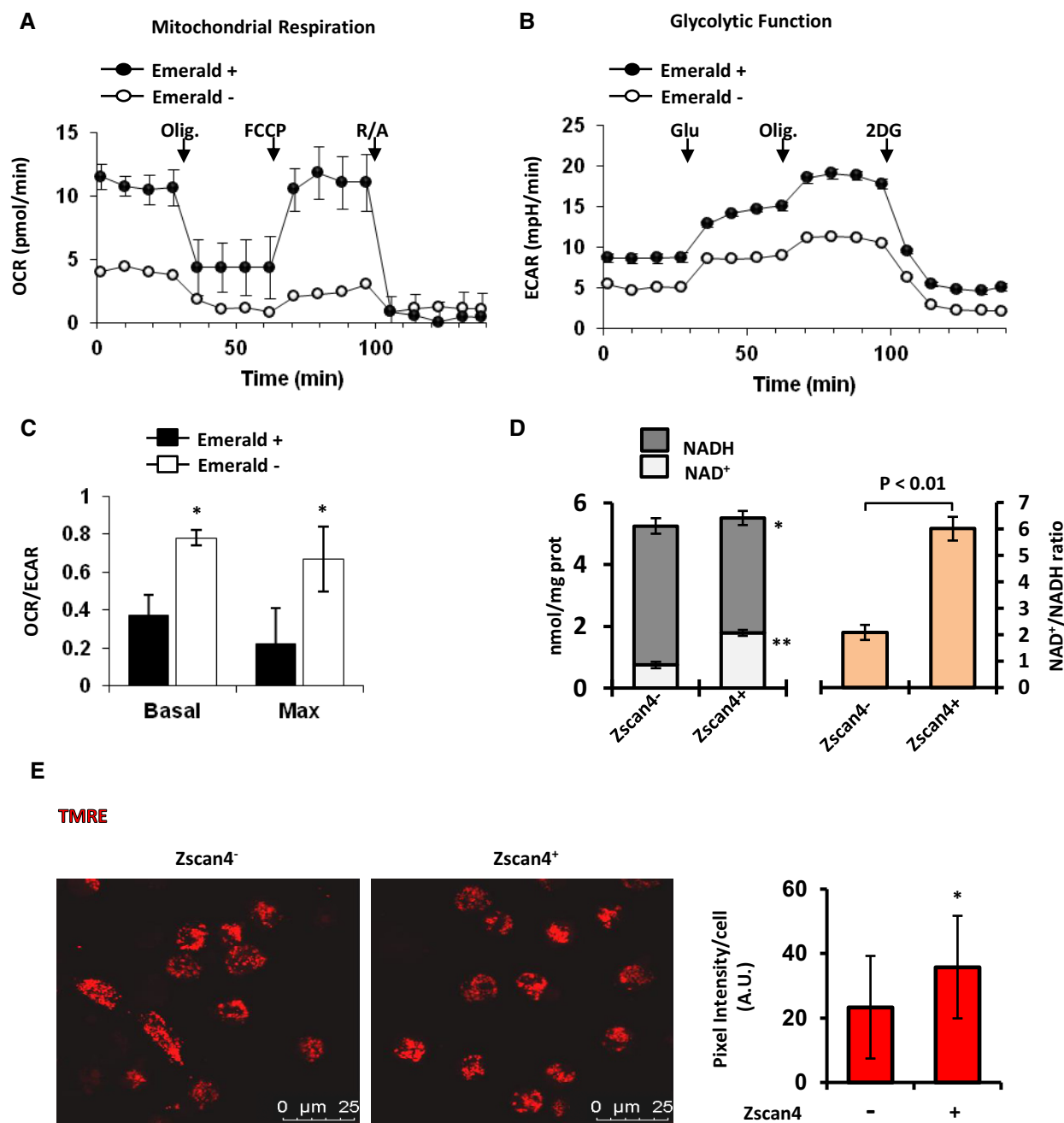


Figure 2. Measurement of metabolic fluxes and mitochondrial respiration-linked parameters in Zscan4⁻ and Zscan4⁺ cells.

A, B Representative seahorse time courses of OCR and ECAR, respectively; where indicated the following compounds were added: oligomycin (olig.), carbonyl cyanide 4-(trifluoromethoxy)phenylhydrazone (FCCP), rotenone plus antimycin A (R/A), glucose (Glu), 2-deoxyglucose (2DG). Each point in the OCR and ECAR time courses is the average ± SD of four technical replicates.

C OCR/ECAR ratio; (4 technical replicates each); Basal, (resting OCR)/(ECAR +Glu); Max, (OCR+FCCP)/(ECAR+Olig.).

D Cellular NAD⁺ and NADH content and NAD⁺/NADH.

E Confocal microscopy analysis of the mitochondrial membrane potential DYm. Pictures on the right, representative imaging of cells loaded with tetramethylrhodamine, ethyl ester (TMRE); histogram on the left, averaged fluorescence intensity/cell ± SD of n = 3 independent biological replicates; *P < 0.05.

Data information: Student's t-test was used for the statistical analysis in panels (C, D, and E). Bar values are means ± SD (E) or ± SEM (C and D) of n = 3 independent biological replicates; *P < 0.05; **P < 0.01 based on NEJM decimal format.

only an adaptation to the energy needs gradually changing according to the cellular state, but it is, instead, a cofactor determining the stem cell identity and fate through metabolites known to be active players in fundamental biological processes such as

epigenetic modifications. In this context, we investigated the metabolic phenotype of the mESC subpopulation characterized by *Zscan4* gene expression to clarify the role of mitochondria in transient metastate.

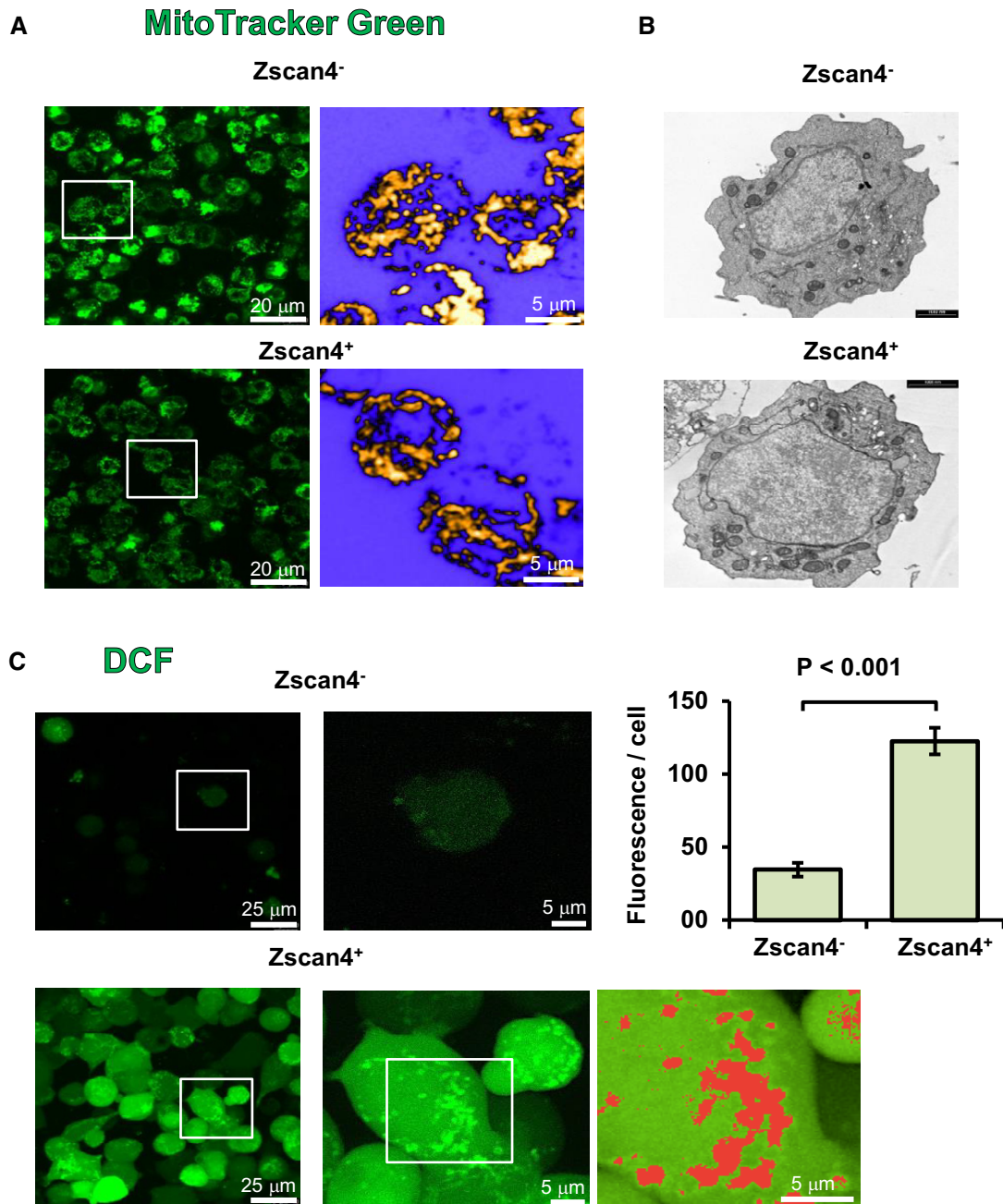


Figure 3. Morpho-functional imaging of *Zscan4*⁻ and *Zscan4*⁺ cells.

A Representative confocal microscopy analysis of cells loaded with MitoTracker Green (pictures on the left); digital enlargements and false colors rendering of details shown as white contoured squares (pictures on the right).

B Electron microscopy images of sorted ES^{Zscan4⁻Emerald} and control cells. Scale bar 1 μ m.

C Representative confocal microscopy analysis of cells loaded with dichlorofluorescein diacetate converted in dichlorofluorescein (DCF) (pictures on the left); digital enlargements and false-color rendering of details shown as white contoured squares (pictures on the right); histogram on the left, averaged fluorescence intensity/cell \pm SEM of $n = 3$ independent biological replicates.

Data information: Student's *t*-test was used for the statistical analysis in panel (C); bar values are means from three independent biological replicates for each of which the fluorescence/cell was averaged from at least ten randomly selected different fields each imaging about 30 cells.

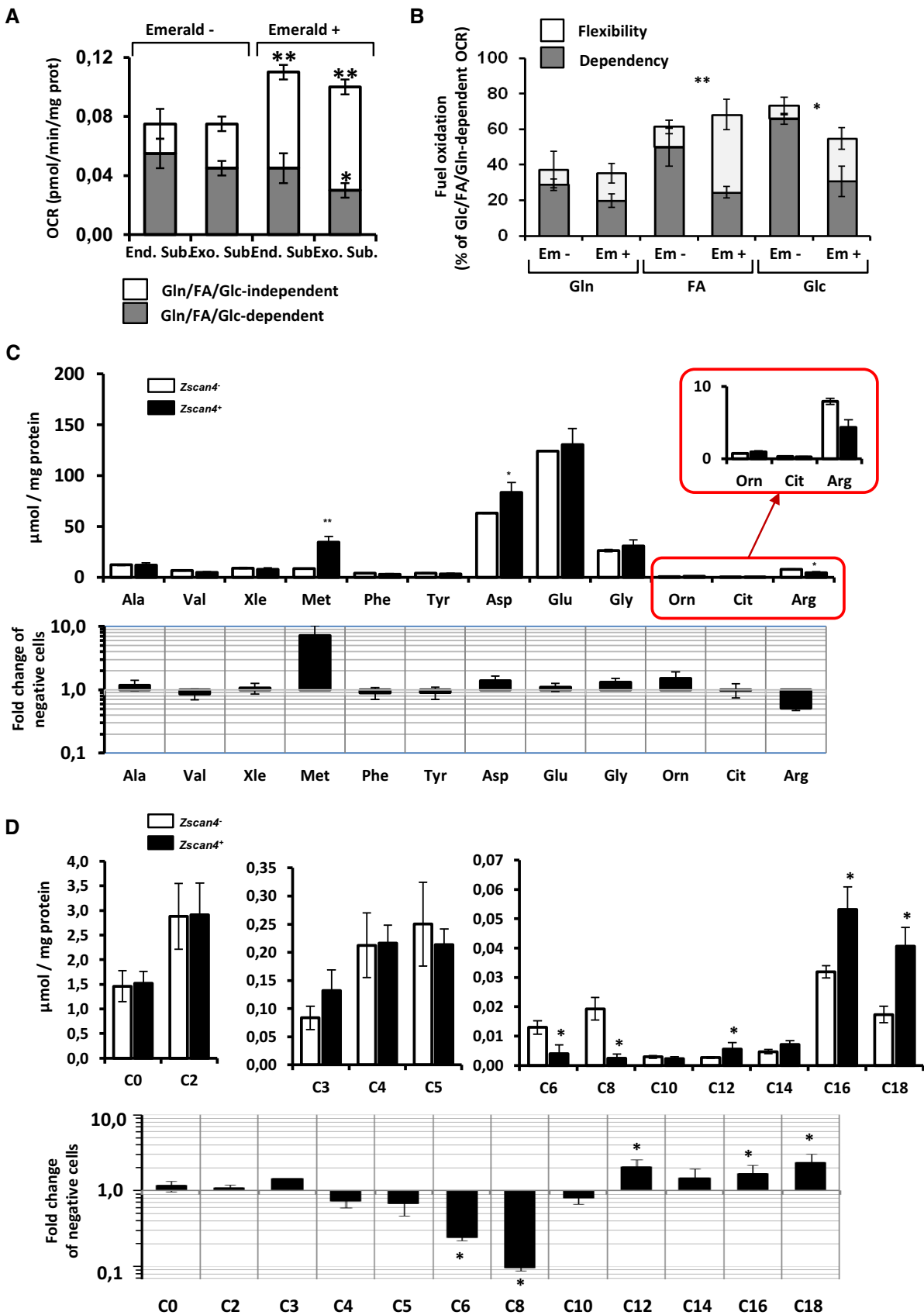


Figure 4.

Figure 4. Analysis of respiratory substrates contribution to mitochondrial OCR and mass spectrometry analysis of free amino acids and acylcarnitine content in *Zscan4⁻* and *Zscan4⁺* cells.

- A Basal R/A-sensitive OCR measured as in Fig 2A in the absence and in the presence of a cocktail of inhibitors (BPTES + etomoxir + UK5099); End. Sub., OCR measured with endogenous substrates; Exo. Sub., OCR measured with glutamine (Gln), fatty acids (FA) and glucose (Glc) supplemented in the assay medium. The superimposed bars are means \pm SEM of $n = 3$ independent biological replicates (3 technical replicates each).
- B Measurement of dependency and flexibility of the OCR to either of Gln, FA, Glc; the assay was carried out according to the MitoFuel protocol (see Materials and Methods); the superimposed bars (whose sum corresponds to the capacity) are means \pm SEM of $n = 3$ independent biological replicates (3 technical replicates each).
- C LC-MSMS analysis of the cellular content of free amino acids; the symbols of amino acids are indicated in x-axis; the amount expressed as $\mu\text{mol}/\mu\text{g}$ protein is indicated in y-axis. The inset shows the content of ornithine, citrulline, and arginine.
- D LC-MSMS analysis of the cellular content of acylcarnitines; the length of the acyl moiety is indicated by the number of carbon atoms in abscissa; bar values are means \pm SEM of $n = 3$ independent biological replicates. The inset shows the content of carnitine (C0) and acetylcarnitine (C2).
- Data information: Student's t-test was used for the statistical analysis in panels (AD). * $P < 0.05$; ** $P < 0.01$ based on NEJM decimal format.

Table 1. Carnitine legend.

C0	Free carnitine
C2	Acetylcarnitine
C3	Propionylcarnitine
C4	Butyrylcarnitine/isobutyrylcarnitine
C5	Isovalerylcarnitine + methylbutyrylcarnitine
C6	Hexanoylcarnitine
C8	Octanoylcarnitine
C10	Decanoylcarnitine
C12	Dodecanoylcarnitine
C14	Tetradecanoylcarnitine
C16	Hexadecanoylcarnitine
C18	Octadecanoylcarnitine

Arginase 2 was previously identified as one of the most upregulated genes in *Zscan4*-expressing mESCs and considered as a reliable marker of the highly pluripotent metastate [14,15]. By competing with the nitric oxide synthase (NOS) for the common L-arginine substrate, arginase 2 contributes to maintaining low levels of nitric oxide (NO) thereby preserving cell survival and delaying differentiation [20,21]. Indeed, in *Zscan4⁺* mESC we have confirmed the upregulation of the mitochondrial-specific arginase 2 isoform along with a reduction of the arginine content and an increase of ornithine level. Firstly, we confirmed the upregulation of the mitochondrial-specific arginase 2 isoform, at the transcript and protein level. Accordingly, compared with *Zscan4⁻* mESC, we found that the arginine content was lower in *Zscan4⁺* mESC, whereas that of ornithine was slightly higher. Thus, we might hypothesize the conversion of arginine in ornithine could fuel the biosynthetic pathway of polyamines such as putrescine, spermidine, and spermine which are involved in a wide array of cellular processes, including the promotion of ESC self-renewal [21–23] histone acetylation, translation, cell reprogramming [24].

Further extension of the amino acids analysis unveiled in *Zscan4⁺* mESC a significantly higher content of methionine and aspartate, whereas all the others detected were present in comparable amounts in the two mESC samples analyzed. Methionine is an essential amino acid critical for epigenetic maintenance: In the presence of ATP, it generates S-adenosylmethionine (SAM) which functions as methyl group donor contributing to DNA and histone methylation thus regulating gene expression. Interestingly, it has

been shown that methionine deprivation reduces NANOG expression promoting ESC differentiation with SAM being the key regulator for maintaining undifferentiated pluripotent stem cells [25]. Metabolites data (Fig EV4) showed that the significant increase of methionine level associated with *Zscan4*-positive cells isolated in RA is not detectable in *Zscan4*-positive cells grown in conventional medium. This is not surprising if we consider that the positive cell population in RM is *Zscan4^{Low}*. RA treatment allows us to obtain and analyze *Zscan4^{High}* enriched cell population showing specific metabolic features to be correlated to the pluripotency state. Since methionine is associated with pluripotency state [25], we conclude that it is coherent with high reprogramming status of *Zscan4*-positive cells in RA (*Zscan4^{High}*).

Moreover, methionine catabolism produces succinyl-CoA that, together with a high level of aspartate, convertible to oxaloacetate, improve the TCA cycle efficiency, ensuring a sufficient number of reduced cofactors, energy, and precursors for purine and pyrimidine synthesis. It is worth mentioning that the 2-oxoglutarate, an intermediate of the TCA cycle, is known to be a cofactor of several chromatin-modifying enzymes, including histone demethylases [26].

Flux analysis resulted in a substantially higher rate of dioxygen consumption in *Zscan4⁺* mESC; this was largely sensitive to the F_0F_1 H^+ -ATP synthase thus indicating that it was coupled to ATP production. Conversely, the lactate-generating glycolytic flux was enhanced to a much lower extent in *Zscan4⁺* mESC. Moreover, we have found (i) a larger NAD⁺/NADH ratio, (ii) an increase of the mitochondrial membrane potential, and (iii) an enhanced level of reactive oxygen species. These results clearly indicate the activation of the aerobic metabolism in *Zscan4⁺* mESCs.

By electron microscopy, however, we did not observe appreciable changes both in number and network morphology of mitochondria albeit they appeared slightly more elongated in *Zscan4⁺* mESCs. However, it must be mentioned that the overproduction of reactive oxidant species observed in *Zscan4⁺* mESC likely remains below the threshold leading to the cytotoxic effect being possibly exploited for triggering mitochondrial biogenesis [27] and redox-sensitive signal pathways including cell proliferation, that appears to be more sustained in these cells. Of note, *Zscan4⁺* mESC shows significant upregulation of glutaredoxin 2, a glutathione-dependent oxidoreductase that facilitates the maintenance of mitochondrial redox homeostasis. Further in-depth investigations are needed to disclose the role of redox signaling in the embryonic stem cell metastate.

Assessment of the respiratory activity in the presence of specific inhibitors of the major oxygen-consuming pathways unveiled in *Zscan4⁺* mESC a greater contribution of substrates other than

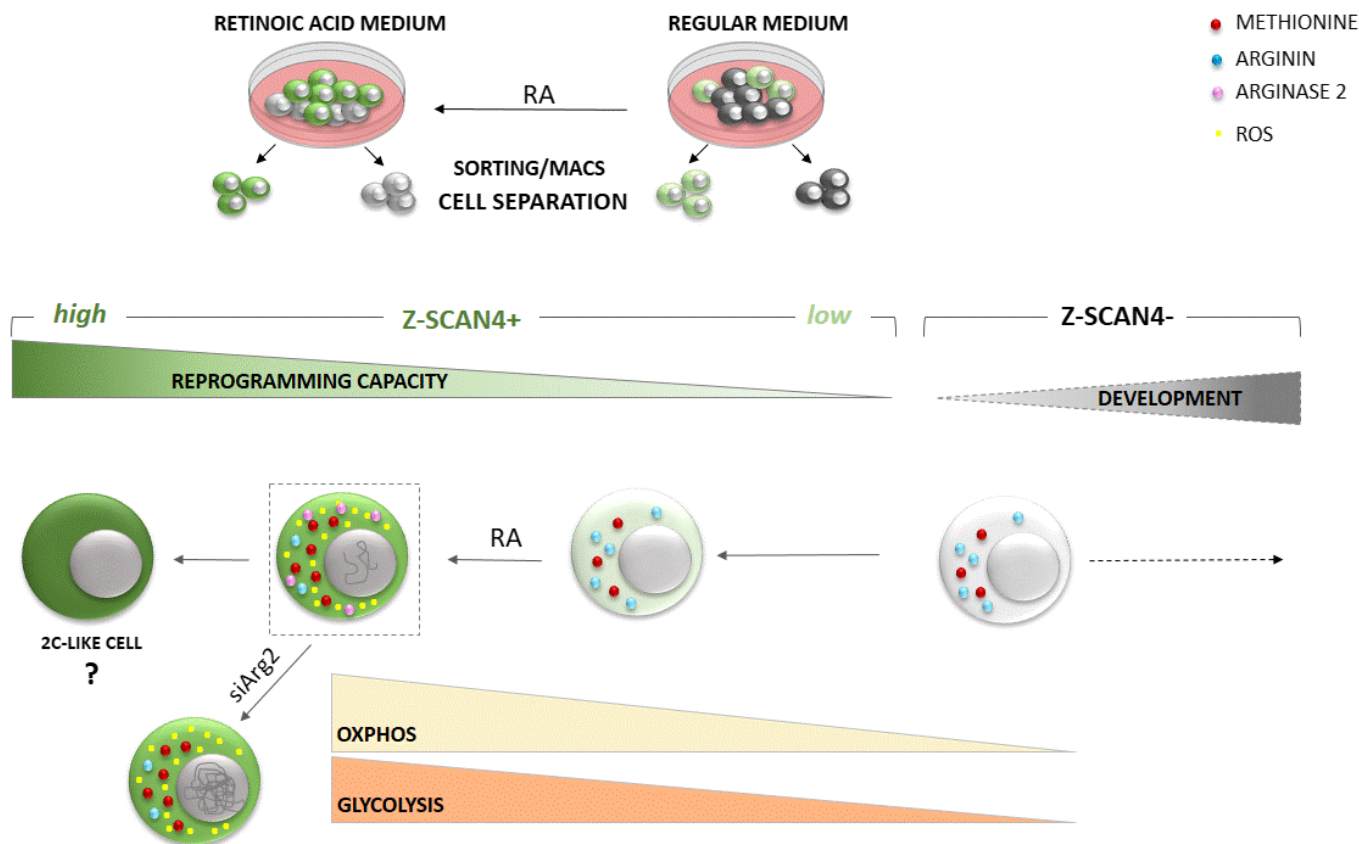


Figure 5. Schematic representation of our study model.

glucose, long-chain fatty acids, and glutamine. However, the identification of the alternative oxidizable metabolites in these cells remains to be established. Interestingly, although the dependence of respiration on fatty acids and glucose was lower in *Zscan4*⁺ mESC, their relative flexibility in the utilization of the two substrates was larger as compared with *Zscan4*⁻ mESC.

Profiling of the acylcarnitine content in both the mESCs resulted in a significant higher levels of C14, C16, C18 in *Zscan4*⁺ cells, likely due to the observed lower consumption of long-chain fatty acids therein, in favor of medium- and short-chain fatty acids whose content resulted indeed to be significantly lower (C4, C5, C6, C8). To note, short-chain fatty acids could function not only as an energy source. Indeed, by-products or intermediates of the mitochondrial beta-oxidation, conjugated to carnitine, can translocate from the cytoplasm to the nucleus thus providing a pool of acetyl-CoA for histone acetylation or may directly inhibit histone deacetylation. We may hypothesize that this would likely result in epigenetic modifications and subsequent regulation of gene expression [28–30].

Materials and Methods

E14tg2^{pcDNA3-prZscan4-EMERALD} culture and flow cytometry sorting

The stably transfected mouse ESCs, derived from strain 129P2/OlaHsd, and generated as in [31], were cultured in gelatin-coated plates in complete ES medium: DMEM (SIGMA); 15% FBS

(EuroClone); 1,000 U/ml leukemia inhibitory factor (LIF) (ESGRO, Chemicon); 1 mM sodium pyruvate; 0.1 mM non-essential amino acids (NEAA), 2.0 mM L-glutamine (Invitrogen), 0.1 mM beta-mercaptoethanol, and 500 U/ml penicillin/streptomycin. ESCs were incubated at 37°C in 5% CO₂.

For differentiation, ESCs were plated in the medium supplemented with 1.5 μM RA for 3 days. For flow cytometry sorting, ESCs were harvested by Trypsin (Gibco) and resuspended in complete ES medium containing 25 mM HEPES buffer. The cells were then FACS-sorted according to the fluorescent intensity of EMERALD into complete ES medium containing HEPES.

E14tg2^{pcDNA3-prZscan4-LNGFR} culture and magnetic separation

The stably transfected mouse ESCs, derived from strain 129P2/OlaHsd and generated as in [13], were cultured for 3 days on gelatin-coated dishes in ES complete medium: GMEM (Sigma) supplemented with 15% FBS (GE Healthcare), L-glutamine 2 mM (Gibco), sodium pyruvate 1 mM (Gibco), MEM amino acids 1× (Gibco), penicillin/streptomycin 100 U-μg/ml (Gibco), 2(β)-mercaptoethanol 0.1 mM (Gibco), LIF 1,000 U/ml (Millipore), G418 137.5 μg/ml. The cells were then trypsinized and plated on gelatin-coated dishes in complete medium with or without 1.5 μM RA for 72 h. For magnetic labeling, single-cell suspensions were centrifuged, resuspended in PBS supplemented with 5 mM EDTA and 0.5% BSA, and incubated with MACSelect^(TM) LNGFR MicroBeads for 15 min on ice. Magnetically labeled cells were isolated over the

AutoMACS Pro Separator (Miltenyi Biotec) with “posseld2” program according to the manufacturer’s protocol. For purity assessment, aliquots of original cell population (magnetically labeled cells before separation), eluted positive (enriched target cells) and negative (untargeted cells collected in the flow-through fraction) cell populations were fluorescently stained with MACSelect Control FITC Antibody (Miltenyi Biotec) that specifically stains MACSelect MicroBead-labeled cells and analyzed by Navios Flow Cytometer (Beckman Coulter).

RNA interference

E14tg2a.4pcDNA3_pZscan4_LNGFR stable cell line was plated (1.7×10^5 well) in 6-well plates and transfected in triplicate with 30 nM Arg2 siGENOME SMART pool siRNA or siGENOME Non-Targeting as scramble control (siCTRL) (Dharmacon, Inc.) after 24 and 72 h from the seeding using the DharmaFECT1 transfection reagent, according to the manufacturer’s procedures. Cells were harvested 96 h after transfection, and the total RNA or total cell lysates were prepared.

RNA extraction RT-PCR and Real-Time Quantitative PCR (RT-qPCR)

RNA was extracted with TRIzol Reagent (Life Technologies) according to the manufacturer’s methods. One microgram of RNA was then reverse transcribed with QuantiTect[®] Reverse Transcription Kit (Qiagen) and used for RT-qPCR with Fast SYBR[®] Master Mix (Applied Biosystem). The number of cycles threshold (Ct) was measured with 7900 Real-Time PCR System (Applied Biosystems). All quantifications (Δ Ct) were normalized with *Gapdh* mRNA level; then, the fold induction was calculated by the $\Delta\Delta$ Ct method [32].

Immunoblotting

Total protein extraction was performed using lysis buffer with 10 mM Tris-HCl (pH 7.5), 1 mM EDTA, 150 mM NaCl, 0.5% NP-40, 1 mM dithiothreitol, 1 mM phenylmethylsulfonyl fluoride, 0.5% sodium deoxycholate, and protease inhibitors. Cell lysates were incubated on ice for 40 min, and the extracts were centrifuged at 15,000 g for 25 min to remove cell debris. Protein concentrations were determined by the Bio-Rad protein assay. After the addition of 4 \times loading buffer (2% sodium dodecyl sulfate [SDS], 30% glycerol, 300 mM β -mercaptoethanol, 100 mM Tris-HCl [pH 6.8]), the samples were incubated at 95°C for 5 min and resolved by SDS-polyacrylamide gel electrophoresis. Proteins were transferred to a PVDF (Millipore, Milan, Italy) and probed with the antibodies. Proteins were visualized by enhanced chemiluminescence (ECL, GE Healthcare, Chicago, IL, USA) and ChemiDoc TM XRS system and analyzed by Quantity One W software (Bio-Rad, Milan, Italy).

Antibodies and reagents

Anti-arginase 2 (GTX118048 Genetex, Irvine, California, USA), Anti-vinculin (7F9), (sc-73614 Santa Cruz Biotechnology, Dallas, TX, USA), anti- β -Actin (C4) (sc-47778, Santa Cruz Biotechnology, Dallas, TX, USA), anti-OPA (ab42364, Abcam, Cambridge, UK), anti-Membrane Integrity Cocktail (ab110414, Abcam,

Cambridge, UK), Anti-Mitofusin 1 [11E91H12] (ab126575, Abcam, Cambridge, UK), Anti-Mitofusin 2 antibody (ab50838, Abcam, Cambridge, UK), anti-DRP1 (#8570, Beverly, Massachusetts), Anti-TOMM20 (ab56783, Abcam, Cambridge, UK), Anti-Tom 40 Polyclonal Antibody (JM-3740-100, MBL, Belgium).

Seahorse XFp

Cellular oxygen consumption (OCR) and extracellular acidification rate (ECAR) measurements in ES^{Zscan4_{Em}} cells stem cells were performed by Seahorse XFp (Seahorse Biosciences, North Billerica, MA, USA), by using Cell Mito Stress Test Kit (cat# 103010-100) and Glycolysis Stress Test Kit (cat # 103017-100), respectively. After FACS-sorting, ES^{Zscan4_{Em}} and control cells were seeded (50,000 cells/well) in miniplates seahorse in ES medium and centrifuged at 300 g for 1 min. Before cell mito stress analyses, the medium was replaced with a buffered base medium (Agilent seahorse-103193) supplemented with 2 mM glutamine, 1 mM pyruvate, and 10 mM glucose at pH 7.4 and equilibrated at 37°C in a CO₂ free incubator for at least 1 h. Basal oxygen consumption rate (OCR) was determined in the presence of glutamine (2 mM) and pyruvate (1 mM). The proton leak was determined after inhibition of mitochondrial ATP production by 1 μ M oligomycin, as an inhibitor of the F₀-F₁ ATPase. Furthermore, the measurement of the ATP production in the basal state it was obtained from the decrease in respiration by inhibition the ATP synthase with oligomycin. Afterward, the mitochondrial electron transport chain was stimulated maximally by the addition of the uncoupler FCCP (1 μ M). Finally, the extra-mitochondrial respiration was estimated after the addition of antimycin A and rotenone (0.5 mM each), inhibitors of the complexes I and III respectively. Coupling efficiency is the proportion of the oxygen consumed to drive ATP synthesis compared with that driving proton leak and was calculated as the fraction of basal mitochondrial OCR used for ATP synthesis (ATP-linked OCR/basal OCR). Spare capacity is the capacity of the cell to respond to an energetic demand and was calculated as the difference between the maximal respiration and basal respiration.

The glycolytic function was obtained by directly measuring the extracellular acidification rate (ECAR) determined using a base medium (Agilent seahorse-103193) supplemented with 2 mM glutamine at pH 7.4. Cells seeded in miniplates were equilibrated at 37°C in a CO₂ free incubator for at least 1 h. The measure of glycolysis was determined in the presence of glutamine 2 mM. The glycolytic capacity, maximum ECAR rate, was determined after the addition of oligomycin (1 μ M). As above, the glycolytic reserve was calculated as the difference between maximal ECAR rate and basal glycolysis. The mitochondrial respiration and glycolytic function were expressed, respectively, as oxygen consumption and extracellular acidification rate per minute normalized to the cells number.

Live cell imaging of mt $\Delta\Psi$ and ROS

Cells cultured at low density on fibronectin-coated 35-mm glass-bottom dishes (Eppendorf, Hamburg, Germany) were incubated for 20 min at 37°C with 2 μ M of TMRE, 10 μ M of DCF, and 100 nM MitoTracker Green (Molecular Probes, Eugene, OR, USA) to monitor mt $\Delta\Psi$, ROS, and mitochondria, respectively. Stained cells were washed with PBS and examined using a Leica TCS SP8 confocal

laser scanning microscope. Acquisition, storage, and data analysis were performed with a dedicated instrumental software from Leica (LAS-X, Wetzlar, Germany).

Ultrastructural observations

Samples were fixed in 3% glutaraldehyde in phosphate buffer (pH 7.2–7.4) for 2 h at room temperature and post-fixed with buffered 1% OsO₄ for 1.5 h at room temperature, dehydrated with ethanol and propylene oxide, and embedded in Spurr's epoxy medium. Ultra-thin (50 nm thick) sections were mounted on 300-mesh copper grids, then stained with uranyl acetate and lead citrate, and observed with a Philips EM 208S TEM.

Metabolite measurements

The cells were collected, counted, and carefully washed. 10×10^6 cells (*ZScan4*⁺ and *ZScan4*⁻) have been pelleted and lysed in cold CH₃OH by using a lysis homogenizer. The mixture was then centrifuged at 15,000 g for 30 min at 4°C. The supernatant was recovered. The protein sediment was resuspended in buffer (7 M urea, 2 M thiourea, 4% Chaps, Tris-HCl 30 mM, and pH 7.5), and protein abundance was determined by Lowry assay. The supernatants were collected, dried under nitrogen, and analyzed to amino acids and acylcarnitine measurements. The dried supernatant was dissolved in methanol containing labeled standards. The metabolites were dissolved in esterifying buffer (3 N hydrochloric acid/n-butanol) at 65°C for 25 min. The samples were dried under nitrogen at 50°C and resuspended in 300 µl of acetonitrile/water (70:30) containing 0.05% formic acid. Three independent aliquots of the sample (100 µl) were injected in the API 4000 triple quadrupole mass spectrometer (AB SCIEX) coupled with an Agilent HPLC system (Agilent Technologies, Waldbronn, Germany) [33]. The LC-MSMS analysis of Ala, Val, Xle, Met, Phe, Tyr, Asp, and Glu was performed by using a Neutral Loss of 102 Da scan function; the other amino acids (Orn, Cyt, Arg, ArgSucc) were analyzed using a Multiple Reaction Monitoring (MRM) experiment. Finally, the AC analysis was performed by a Precursor Scan of 85 Da fragments [34].

Quantitative analyses were performed by using ChemoView v.1.2 software (Sciex, Framingham, MA, USA). Final acylcarnitine and amino acid concentrations were calculated based on 0.1 mg protein from the cellular extract [35]. Data are expressed as means ± SEM. Statistical differences of normally distributed data between 2 treatments were determined by using an unpaired Student's *t*-test by using Prism 5.0 (GraphPad Software, La Jolla, CA, USA). Differences between treatments were considered significant at a value of $P < 0.05$.

Acquisition and analysis on the ImageStream^X Mark II

Imaging flow cytometry was performed on an ImageStream^X Mark II with INSPIRE (version 200.1.388.0) acquisition software (Amnis Merck, Seattle, USA). Briefly, *Zscan4*⁺ siArg2 and *Zscan4*⁺ siCtrl cells were stained by labeling histone H3 protein and defining nuclear region with DAPI. Specifically, after permeabilization with TX-100 0.2% for 10 min, cells were incubated with a specific antibody anti-H3 (06-755 Merck KGaA) revealed with a secondary FITC-

conjugated antibody. Prior to acquisition, samples were filtered using a filter of 50 µm in order to remove aggregates. Cells were collected with high sensitivity and low flow rate at 60× magnification; 488 and 405 nm lasers with brightfield and darkfield light source turned on. Fluorescent signals were collected into different channels. Data were acquired at an average rate of 10–30 events per second, in samples containing 5×10^5 cells each. The acquired raw image file (.rif) contain 2,000 events. Power laser and range of pixel intensity were defined before their collection with INSPRE software, in order to avoid saturated signals and to fine-tune the image display, respectively.

The acquired raw image file was analyzed with IDEAS software (version 6.2.64.0) generating a compensated image file (.cif) and afterward data analysis file (.daf). In the analysis, the following gating strategy was employed: (a) the cells with better focus were selected, using gradient RMS feature; (b) in order to consider single cells, a dot plot showing area versus aspect ratio (AR) was created, removing events with AR less than one.

The intensity of H3 fluorescent signal was measured in the nuclear region by creating a mask defined by DAPI staining. The texture feature of fluorescent signal was analyzed by using the modulation method, which measures the fluorescence intensity range of an image as described by the formula: Modulation = Max Pixel – Min Pixel/Max Pixel + Min Pixel. We have distinguished two cell populations (R1 and R2) corresponding to two different patterns of fluorescent signal: homogenous and clustered distribution, respectively. We defined the threshold between the two populations on the control samples, and the same gate was applied to analyze the Arg2 knockdown cells.

Statistical analysis

Statistical analyses were performed using GraphPad Prism7 (GraphPad Software Inc). Data are shown as mean ± SEM or ± SD as indicated in figure legends. Statistical significance of the difference in measured variables among samples was determined by two tailed unpaired *t*-test with Welch's correction when two groups were compared, while, when more than two groups were compared, one-way or two-way ANOVA with Brown-Forsythe corrections was performed. Number of samples per group and number of independent experiments are described in figure legends. To minimize the effects of subjective bias, the results were evaluated independently by the 4 active authors. In particular, the experiments conducted to assess the metabolic phenotype were performed independently in two different Research Institutes. To report *P*-values, the NEJM (New England Journal of Medicine) decimal format was used; differences were considered statistically significant at * $P < 0.05$, ** $P < 0.01$, *** $P < 0.001$.

Expanded View for this article is available online.

Acknowledgements

We would like to thank prof. Basile Adriana and her technical assistant dr. Sergio Sorbo for helping us with electron microscopy experiments. This work was supported by Biogem, Istituto di Biologia e Genetica Molecolare, Via Camporeale, Ariano Irpino (AV), STAR Linea 1, 2014 (University of Naples Federico II), InterOmics 2017 "PROPAGA" (IEOS, CNR) to GF, PRIN 2017 (ENTI DI RICERCA DI RILEVANTE INTERESSE NAZIONALE)—Prot.2017XJ38A4.

Author contributions

AT: Design of the experiments, analysis and interpretation of the data, writing of the article. CPa: Design of the experiments, analysis and interpretation of the data, writing of the article. VR, MAVL: Cell culture, cell sorting and cell line engineering. RS, FA, FT, PL: Mitochondrial activity and ROS analysis. GC, MPM: Seahorse data generation and interpretation. MC, MR: Metabolic data, LC-MSMS analysis, interpretation of data. SP, DS, FV: Immunofluorescence analysis and electronic microscopy interpretation. VC, NC, CPI, GF: contributed to write the paper. CPI: writing, critical revision and discussion, design of the experiments. GF: conception and design of the experiments, writing, critical revision.

Conflict of interest

The authors declare that they have no conflict of interest.

References

- Morey L, Santanach A, Di Croce L (2015) Pluripotency and epigenetic factors in mouse embryonic stem cell fate regulation. *Mol Cell Biol* 35: 2716–2728
- Jiang J, Lv W, Ye X, Wang L, Zhang M, Yang H, Okuka M, Zhou C, Zhang X, Liu L et al (2013) Zscan4 promotes genomic stability during reprogramming and dramatically improves the quality of iPSCs as demonstrated by tetraploid complementation. *Cell Res* 23: 92–106
- Hisada K, Sánchez C, Endo TA, Endoh M, Román-Trufero M, Sharif J, Koseki H, Vidal M (2012) RYBP represses endogenous retroviruses and preimplantation- and germ line-specific genes in mouse embryonic stem cells. *Mol Cell Biol* 32: 1139–1149
- Rodriguez-Terrones D, Gaume X, Ishiuchi T, Weiss A, Kopp A, Kruse K, Penning A, Vaquerizas JM, Brino L, Torres-Padilla ME (2018) A molecular roadmap for the emergence of early-embryonic-like cells in culture. *Nat Genet* 50: 106–119
- Hendrickson PG, Dorais JA, Grow EJ, Whiddon JL, Lim JW, Wike CL, Weaver BD, Pflueger C, Emery BR, Wilcox AL et al (2017) Conserved roles of mouse DUX and human DUX4 in activating cleavage-stage genes and MERVL/HERVL retrotransposons. *Nat Genet* 49: 925–934
- Kalmbach K, Robinson LG, Wang F, Liu L, Keefe D (2014) Telomere length reprogramming in embryos and stem cells. *Biomed Res Int* 2014: 925121
- Eckersley-Maslin MA, Svensson V, Krueger C, Stubbs TM, Giehr P, Krueger F, Eckersley-Maslin MA, Svensson V, Krueger C, Stubbs TM et al (2016) MERVL/Zscan4 network activation results in transient genome-wide DNA demethylation of mESCs. *Cell Rep* 17: 179–192
- Zeng F, Schultz RM (2005) RNA transcript profiling during zygotic gene activation in the preimplantation mouse embryo. *Dev Biol* 283: 40–57
- Li L, Zheng P, Dean J (2010) Maternal control of early mouse development. *Development* 137: 859–870
- Nagaraj R, Sharpley MS, Chi F, Braas D, Zhou Y, Kim R, Clark AT, Banerjee U (2017) Nuclear localization of mitochondrial TCA cycle enzymes as a critical step in mammalian zygotic genome activation. *Cell* 168: 210–23.e11
- Moussaieff A, Rouleau M, Kitsberg D, Cohen M, Levy G, Barasch D, Nemirovski A, Shen-Orr S, Laevsky I, Amit M et al (2015) Glycolysis-mediated changes in acetyl-CoA and histone acetylation control the early differentiation of embryonic stem cells. *Cell Metab* 21: 392–402
- Gu W, Gaeta X, Sahakyan A, Chan AB, Hong CS, Kim R, Braas D, Plath K, Lowry WE, Christofk HR (2016) Glycolytic metabolism plays a functional role in regulating human pluripotent stem cell state. *Cell Stem Cell* 19: 476–490
- Tagliaferri D, Mazzone P, Noviello TMR, Addeo M, Angrisano T, Del Vecchio L, Visconte F, Ruggieri V, Russi S, Caivano A et al (2020) Retinoic acid induces embryonic stem cells (ESCs) transition to 2 cell-like state through a coordinated expression of Dux and Duxbl1. *Front Cell Dev Biol* 7: 385
- Morris SM Jr (2004) Enzymes of arginine metabolism. *J Nutr* 134: 2743S–2747S; discussion 65S–67S
- Cerulo L, Tagliaferri D, Marotta P, Zoppoli P, Russo F, Mazio C, DeFelice M, Ceccarelli M, Falco G (2014) Identification of a novel gene signature of ES cells self-renewal fluctuation through system-wide analysis. *PLoS ONE* 9: e83235
- Tagliaferri D, De Angelis MT, Russo NA, Marotta M, Ceccarelli M, Del Vecchio L, De Felice M, Falco G (2016) Retinoic acid specifically enhances embryonic stem cell metastate marked by Zscan4. *PLoS ONE* 11: e0147683
- Akiyama T, Xin L, Oda M, Sharov AA, Amano M, Piao Y, Cadet JS, Dudekula DB, Qian Y, Wang W et al (2015) Transient bursts of Zscan4 expression are accompanied by the rapid derepression of heterochromatin in mouse embryonic stem cells. *DNA Res* 22: 307–318
- Dan J, Yang J, Liu Y, Xiao A, Liu L (2015) Roles for histone acetylation in regulation of telomere elongation and two-cell state in mouse ES cells. *J Cell Physiol* 230: 2337–2344
- Lees JG, Gardner DK, Harvey AJ (2017) Pluripotent stem cell metabolism and mitochondria: beyond ATP. *Stem Cells Int* 2017: 2874283
- Lisowski P, Kannan P, Mlody B, Prigione A (2018) Mitochondria and the dynamic control of stem cell homeostasis. *EMBO Rep* 19: e45432
- Tejedo JR, Tapia-Limonchi R, Mora-Castilla S, Cahuana GM, Hmadcha A, Martin F, Bedoya FJ, Soria B (2010) Low concentrations of nitric oxide delay the differentiation of embryonic stem cells and promote their survival. *Cell Death Dis* 1: e80
- Zhao T, Goh KJ, Ng HH, Vardy LA (2012) A role for polyamine regulators in ESC self-renewal. *Cell Cycle* 11: 4517–4523
- James C, Zhao TY, Rahim A, Saxena P, Muthalif NA, Uemura T, Tsuneyoshi N, Ong S, Igarashi K, Lim CY et al (2018) MINDY1 is a downstream target of the polyamines and promotes embryonic stem cell self-renewal. *Stem Cells* 36: 1170–1178
- Miller-Fleming L, Olin-Sandoval V, Campbell K, Ralser M (2015) Remaining mysteries of molecular biology: the role of polyamines in the cell. *J Mol Biol* 427: 3389–3406
- Shiraki N, Shiraki Y, Tsuyama T, Obata F, Miura M, Nagae G, Aburatani H, Kume K, Endo F, Kume S (2014) Methionine metabolism regulates maintenance and differentiation of human pluripotent stem cells. *Cell Metab* 19: 780–794
- Tran KA, Dillingham CM, Sridharan R (2019) The role of alpha-ketoglutarate-dependent proteins in pluripotency acquisition and maintenance. *J Biol Chem* 294: 5408–5419
- Piantadosi CA, Suliman HB (2012) Redox regulation of mitochondrial biogenesis. *Free Radic Biol Med* 53: 2043–2053
- Taylor EM, Jones AD, Henagan TM (2014) A review of mitochondrial-derived fatty acids in epigenetic regulation of obesity and type 2 diabetes. *J Nutr Health Food Sci* 2: 1–4
- Sabari BR, Zhang D, Allis CD, Zhao Y (2017) Metabolic regulation of gene expression through histone acylations. *Nat Rev Mol Cell Biol* 18: 90–101
- Napolitano G, Tagliaferri D, Fusco S, Cirillo C, De Martino I, Addeo M, Mazzone P, Russo NA, Natale F, Cardoso MC et al (2020) A novel member of Prame family, Gm12794c, counteracts retinoic acid

- differentiation through the methyltransferase activity of PRC2. *Cell Death Differ* 27: 345–362
31. Zalzman M, Falco G, Sharova LV, Nishiyama A, Thomas M, Lee SL, Stagg CA, Hoang HG, Yang HT, Indig FE *et al* (2010) Zscan4 regulates telomere elongation and genomic stability in ES cells. *Nature* 464: 858–863
 32. Falco G, Stanghellini I, Ko MS (2006) Use of Chuk as an internal standard suitable for quantitative RT-PCR in mouse preimplantation embryos. *Reprod Biomed Online* 13: 394–403
 33. Ruoppolo M, Caterino M, Albano L, Pecce R, Di Girolamo MG, Crisci D, Costanzo M, Milella L, Franconi F, Campesi I (2018) Targeted metabolomic profiling in rat tissues reveals sex differences. *Sci Rep* 8: 4663
 34. Ruoppolo M, Scolamiero E, Caterino M, Mirisola V, Franconi F, Campesi I (2015) Female and male human babies have distinct blood metabolomic patterns. *Mol BioSyst* 11: 2483–2489
 35. Ruoppolo M, Campesi I, Scolamiero E, Pecce R, Caterino M, Cherchi S, Mercurio G, Tonolo G, Franconi F (2014) Serum metabolomic profiles suggest influence of sex and oral contraceptive use. *Am J Transl Res* 6: 614–624